Flow Turbulence Combust (2013) 91:541–563
DOI 10.1007/s10494-013-9459-7

An Assessment of Dynamic Subgrid-Scale Sea-Surface Roughness Models

Di Yang · Lian Shen · Charles Meneveau

Received: 15 October 2012 / Accepted: 7 April 2013 / Published online: 23 April 2013

Abstract Covered by waves with various lengths, the mobile sea surface represents a great challenge to the large-eddy simulation (LES) of atmospheric boundary layer flow over the ocean surface. In this study, we report recent developments and tests of dynamic modeling approaches for the subgrid-scale (SGS) sea-surface roughness for LES. In the model, introduced originally in Yang et al. (J. Fluid Mech., in press, 2013), the SGS roughness is quantified by an integral of the SGS wave spectrum, σ_η^Δ, weighted based on the wind-wave kinematics, with an unknown model coefficient α_w as pre-factor. The coefficient α_w is determined dynamically based on the basic constraint that the total surface drag force must be independent of the LES filter scale. The weighted integral σ_η^Δ represents the effective amplitude of the SGS waves, for which five candidate models are reviewed. Following the computational tests presented in Yang et al. (J. Fluid Mech., in press, 2013), in this study the performance of the dynamic SGS sea-surface roughness models is assessed by a theoretical approach, in which the roughness model is coupled with the critical-layer theory of wind–wave interaction. This theoretical approach mimics the averaged behavior of the LES. Meanwhile, its low computation cost allows the assessment of the model

Submitted for FTC Special Issue ETMM9.

D. Yang · C. Meneveau (✉)
Department of Mechanical Engineering, Johns Hopkins University,
Baltimore, MD 21218, USA
e-mail: meneveau@jhu.edu

L. Shen
Department of Mechanical Engineering, University of Minnesota,
Minneapolis, MN 55455, USA

L. Shen
St. Anthony Falls Laboratory, University of Minnesota, Minneapolis, MN 55414, USA

C. Meneveau
Center for Environmental and Applied Fluid Mechanics, Johns Hopkins University,
Baltimore, MD 21218, USA

performance over a wide range of parameters. The test results indicate that the dynamic modeling approach can reliably model the roughness length of the SGS waves without ad-hoc prescription of the model parameter α_w. Also, we confirm that to model σ_η^Δ, an expression based on the kinematics of wind–wave relative motion achieves the best performance among the five candidate models considered.

Keywords Sea-surface roughness · Turbulence modeling · Wind–wave interaction · Critical-layer theory

1 Introduction

Turbulence over rough surfaces is of vital importance to many environmental and engineering applications. Among various types of rough surfaces, an important class is the rough surfaces that have multiscale, fractal-like geometries. Such rough surfaces widely exist especially in the natural environment. Examples include evolved fluvial landscapes [42], tree canopies [11, 12], and the wind-driven sea surface [9]. Among them, perhaps the most challenging case is the atmospheric boundary layer flow over ocean waves. Due to wind excitation, the sea surface is covered by roughness elements, the waves, with a wide range of wavelengths. Governed by the wave dispersion relation, the waves with different wavelengths propagate at different speeds relative to the wind, interacting with the turbulent wind in the atmospheric boundary layer in a complex manner. The wind–wave interaction problem has attracted great attention because of its critical role in weather forecasting, naval architecture, ocean and coastal engineering, and offshore wind and wave energy.

In recent years, large-eddy simulation (LES) has become an important research tool for the study of atmospheric boundary layer flows over rough sea surface. However, performing LES for such flows is a challenging task. The wind-driven sea surface exhibits a power-law type spectrum over a wide range of scales [20]. At most, typically only a part of the surface wave spectrum falls above the grid scale (GS) of the LES and is resolved in the simulation. The waves in the subgrid scale (SGS) range, on the other hand, are unresolved in the LES and must be parameterized, e.g. using the concept of the SGS surface roughness length $z_{0,\Delta}$. (Here and hereinafter, 'Δ' denotes the grid size in the LES.) The surface stress due to the SGS roughness is usually imposed to the LES as a boundary condition through the log-law surface-layer model [5, 6, 45, 46]. However, the choice of $z_{0,\Delta}$ heavily relies on pre-tabulated values from experiments. The measurement data are often limited or highly scattered, and may not be suitable when the flow conditions change (see the reviews in references [15, 24, 51]).

Recently, Anderson and Meneveau [2] have developed a dynamic method for the modeling of SGS surface roughness for turbulence over multiscale, fractal-like static land surfaces. In their model, the SGS surface roughness is modeled as $z_{0,\Delta} \sim \alpha_w \sigma_\eta^\Delta$. Here, σ_η^Δ, the effective amplitude of the SGS surface roughness, was chosen to equal to the root-mean-square (r.m.s.) value of the SGS height fluctuations; and α_w, called the roughness index, is an unknown model coefficient. The total stress on the rough surface consists of a GS part and an SGS part. The key concept of the dynamic model is to enforce the constraint that the total surface stress must be invariant with respect

to the filter scale in the LES. As reviewed in reference [36], this approach can be considered as a generalization of the Germano identity and the dynamic model [18] used in modeling SGS stresses in turbulent flows. The unknown coefficient α_w is thus determined by solving the equation that equalizes the total surface stresses at the grid scale Δ and a test-filter scale, say, 2Δ. This dynamic process of determining α_w overcomes the ambiguity in traditional LES that prescribes the SGS surface roughness value *ad hoc*. The dynamic SGS surface roughness model has been shown to work well for LES of turbulent flows over rough multiscale land surfaces with power-law surface spectra [2] and over fluvial-like landscapes [3].

By taking advantage of the recent development in the numerical simulation of wind–wave interaction [53–56], Yang et al. [57] extended the dynamic SGS surface roughness model to the sea-surface problem. They showed that, compared with the static land surfaces, the modeling of σ_η^Δ for the SGS waves on the sea surface is more challenging. By reviewing previous studies on the modeling of sea-surface roughness, they proposed four models for σ_η^Δ in addition to the RMS model used by Anderson and Meneveau [2], namely, the geometry model, the steepness-dependent Charnock model, the wave-kinematics-dependent model, and the combined-kinematics-steepness model. The dynamic approach and the five models of σ_η^Δ were tested by means of a priori and a posteriori tests. Satisfactory results were obtained for the three wind-wave conditions considered in their study, with best results observed for the wave-kinematics-dependent model.

In the present study, the performance of the dynamic SGS sea-surface roughness models is further assessed, but using a different, theoretical, tool. The 1993 critical-layer theory of Miles [39] is adopted for the modeling of wind–wave interaction. The theory is applied to the broadband wave condition to predict the GS surface stress (i.e. the pressure-induced form drag), which is then combined with the dynamic modeling of SGS sea-surface roughness to mimic the statistical behavior of an actual LES. The value of sea-surface roughness obtained from such a mimicked 'simulation' is then compared with the benchmark value, which is obtained by the prediction purely based on the critical-layer theory.

Note that the computational cost of the current theoretical assessment is significantly lower than that of actual LES runs. This feature allows us to perform the test of dynamic SGS sea-surface roughness models over a much broader range of parameters than what LES runs can afford. In this paper, four different wind conditions are considered, including $U_{10} = 4, 6, 8$, and 10 m/s, where U_{10} is the mean wind velocity at the height of 10 meters above the mean water level. Moreover, a wide range of fetch F is considered, from 0.5 to 500 km continuously, which covers most of the stages in the development of sea-surface gravity waves under wind forcing. Here, fetch F is the distance of wind blowing over sea surface. For each (U_{10}, F) condition, three different grid-filter scales are also considered to test the resolution independency of the dynamic SGS roughness model. The current study helps to achieve a rather comprehensive evaluation of the dynamic SGS roughness models.

This paper is organized as follows. The dynamic models of SGS sea-surface roughness are presented in Section 2. In Section 3, the critical-layer theory for modeling wind–wave interaction is discussed, and is applied to obtain the benchmark evaluation of the sea-surface roughness. In Section 4, the dynamic SGS roughness modeling approach is tested by the coupling with the critical-layer theory, and the

test result for the various candidate models is discussed. Finally, the conclusions and discussion are presented in Section 5.

2 Dynamic Modeling of SGS Sea-Surface Roughness for LES

2.1 Review of dynamic modeling procedure

For a three-dimensional LES of wind turbulence over waves, let $x_i(i = 1, 2, 3) = (x, y, z)$, where x and y are horizontal coordinates and z is the vertical coordinate, with $z = 0$ being the mean water level. Also let $\widetilde{u}_i(i = 1, 2, 3) = (\widetilde{u}, \widetilde{v}, \widetilde{w})$ be the velocity components in x-, y-, and z-directions, respectively. Here, $(\widetilde{...})$ indicates filtering at the grid scale, Δ, in LES. The horizontal-averaged total streamwise sea-surface stress acting on the wind at the sea surface can be written as

$$\langle \tau^T_{13,\Delta} \rangle = \underbrace{-\frac{1}{\mathcal{A}} \iint_{\mathcal{A}} \widetilde{p}\, \frac{\partial \widetilde{\eta}}{\partial x}\, \mathrm{d}A}_{\langle \tau^{GS}_{13,\Delta} \rangle} + \underbrace{\frac{\rho_a}{\mathcal{A}} \iint_{\mathcal{A}} \tau^{SGS}_{13,\Delta}\, \mathrm{d}A}_{\langle \tau^{SGS}_{13,\Delta} \rangle} . \tag{1}$$

Here, $\tau^{GS}_{13,\Delta}$ and $\tau^{SGS}_{13,\Delta}$ represent the surface stresses due to the GS and SGS waves, respectively; $\langle ... \rangle$ denotes the horizontal averaging; $\mathcal{A}$ is the sea-surface area; η is the sea-surface elevation; $\widetilde{p}$ is the resolved air pressure on the sea surface; and ρ_a is the air density. For flow conditions typical of atmospheric boundary layers, the Reynolds number is sufficiently high so that the viscous stress at and above the scale Δ is negligible.

The SGS kinematic surface stress $\tau^{SGS}_{13,\Delta}$ is modeled by a logarithmic surface-layer model based on the Monin–Obukhov similarity theory [41], which can be written as [1, 5, 6, 40]

$$\tau^{SGS}_{13,\Delta}(x, y, t) = -\left[\frac{\kappa \widehat{\widetilde{U}}_r(x, y, t)}{\log\left(\frac{d_2}{z_{0,\Delta}}\right)} \right]^2 \frac{\widehat{\widetilde{u}}_r(x, y, t)}{\widehat{\widetilde{U}}_r(x, y, t)} . \tag{2}$$

Here, κ is the von Kármán constant; $(\widehat{\widetilde{...}})$ indicates filtering at the test-filter scale 2Δ; $z_{0,\Delta}$ is the roughness scale associated with SGS waves; and

$$\widehat{\widetilde{U}}_r(x, y, t) = \sqrt{\left[\widehat{\widetilde{u}}_r(x, y, t)\right]^2 + \left[\widehat{\widetilde{v}}_r(x, y, t)\right]^2} , \tag{3}$$

where $\widehat{\widetilde{u}}_{r,i}(i = 1, 2) = (\widehat{\widetilde{u}}_r, (\widehat{\widetilde{v}}_r)$ are the air velocities relative to the water surface at the first off-surface grid-point (in Eq. 2, d_2 is the vertical distance of the first off-surface grid-point to the surface in the LES), i.e.

$$\widehat{\widetilde{u}}_{r,i}(x, y, t) = \widehat{\widetilde{u}}_i(x, y, d_2, t) - \widehat{\widetilde{u}}_{s,i}(x, y, t) , \quad i = 1, 2 , \tag{4}$$

with $\widehat{\widetilde{u}}_{s,i}(x, y, t)$ being the sea-surface velocity. Note that, the logarithmic law in Eq. 2 was originally obtained in an averaged sense. To apply it locally, in Eq. 2 the test-filtered velocities at the scale 2Δ have been used instead of the grid-resolved velocities. This treatment has been shown to help suppress excessive velocity fluctuations and improve the applicability and numerical stability of Eq. 2 (see reference [5] for detailed discussion).

The SGS sea-surface roughness length $z_{0,\Delta}$ in Eq. 2 is modeled as [2]

$$z_{0,\Delta} = \sqrt{z_{0,s}^2 + \left(\alpha_w \, \sigma_\eta^\Delta\right)^2} \, . \tag{5}$$

Here,

$$z_{0,s} = 0.11 \nu_a / u_* \tag{6}$$

is the roughness for a smooth surface, with ν_a being the kinematic viscosity of air and u_* being the friction velocity of wind; and σ_η^Δ is the effective amplitude of the SGS waves. The modeling of σ_η^Δ is discussed in detail in Section 2.2.

The dynamic method uses the fundamental constraint that the horizontal-averaged total streamwise surface stress $\langle \tau_{13,\Delta}^T \rangle$ must be invariant with respect to the filter scale. Equalizing $\langle \tau_{13}^T \rangle$ at grid-filter scale Δ and test-filter scale 2Δ gives

$$\underbrace{-\frac{1}{\mathcal{A}} \iint_{\mathcal{A}} \widetilde{p} \, \frac{\partial \widetilde{\eta}}{\partial x} \, \mathrm{d}A}_{\langle \tau_{13,\Delta}^{GS} \rangle} \underbrace{- \frac{\rho_a}{\mathcal{A}} \iint_{\mathcal{A}} \left[\frac{\kappa \, \widehat{\widetilde{U}}_r}{\log\left(\frac{d_2}{\sqrt{z_{0,s}^2 + (\alpha_w \sigma_\eta^\Delta)^2}} \right)} \right]^2 \frac{\widehat{\widetilde{u}}_r}{\widehat{\widetilde{U}}_r} \, \mathrm{d}A}_{\langle \tau_{13,\Delta}^{SGS} \rangle}$$

$$= \underbrace{-\frac{1}{\mathcal{A}} \iint_{\mathcal{A}} \widehat{\widetilde{p}} \, \frac{\partial \widehat{\widetilde{\eta}}}{\partial x} \, \mathrm{d}A}_{\langle \tau_{13,2\Delta}^{GS} \rangle} \underbrace{- \frac{\rho_a}{\mathcal{A}} \iint_{\mathcal{A}} \left[\frac{\kappa \, \overline{\widehat{\widetilde{U}}}_r}{\log\left(\frac{d_2}{\sqrt{z_{0,s}^2 + (\alpha_w \sigma_\eta^{2\Delta})^2}} \right)} \right]^2 \frac{\overline{\widehat{\widetilde{u}}}_r}{\overline{\widehat{\widetilde{U}}}_r} \, \mathrm{d}A}_{\langle \tau_{13,2\Delta}^{SGS} \rangle} \, . \tag{7}$$

Here, $\overline{\widehat{\widetilde{(\ldots)}}}$ indicates filtering at a second test-filter scale 4Δ; and $\overline{\widehat{\widetilde{U}}}_r = \left[(\overline{\widehat{\widetilde{u}}}_r)^2 + (\overline{\widehat{\widetilde{v}}}_r)^2 \right]^{1/2}$. The use of twice test-filtering for the velocities on the right hand side of Eq. 7 is also for the sake of reducing excessive velocity fluctuations and improving its applicability in the localized manner, the same as in Eq. 2 (for detailed discussion, see references [2, 5]). In the dynamic model, the roughness index α_w is assumed to be invariant with respect to the filter in LES [2], and is obtained by solving Eq. 7.

2.2 Candidate models for σ_η^Δ

In this study, the information of surface η is assumed to be available at all of the scales, i.e. the wave spectrum is assumed known. This is a legitimate assumption, because nowadays the wave field can be computed with very high resolution using advanced nonlinear wave simulation method such as the high-order spectral method [13, 35, 56, 57]. In practice, the wind-generated waves can also be described by the measured wave spectra such as the one obtained during the Joint North Sea Wave Observation Project (JONSWAP) [20]:

$$S(k) = \frac{\alpha_P}{2k^3} \exp\left[-\frac{5}{4} \left(\frac{k_p}{k} \right)^2 \right] \gamma^{\exp \frac{-(\sqrt{k} - \sqrt{k_p})^2}{2\sigma^2 k_p}} \, , \tag{8}$$

where

$$\alpha_P = 0.076 \left(\frac{U_{10}^2}{gF} \right)^{0.22} , \tag{9}$$

$$k_p = \left[g \left(\frac{22}{U_{10} F} \right)^2 \right]^{1/3} , \tag{10}$$

$$\gamma = 3.3 , \tag{11}$$

$$\sigma = \begin{cases} 0.07 & k \le k_p , \\ 0.09 & k > k_p . \end{cases} \tag{12}$$

Here, k_p is the wavenumber at the spectrum peak; g is the gravitational acceleration; α_P is the Phillips coefficient; and γ is the peak enhancement factor. Figure 1 illustrates the JONSWAP wavefield for the condition of $U_{10} = 6\,\text{m/s}$ and $F = 50\,\text{km}$.

In the dynamic modeling of the SGS sea-surface roughness, a key challenge is how to model the effective amplitude of SGS waves, σ_η^Δ, based on the wave characteristics. Yang et al. [57] proposed five candidate models after reviewing the previous parameterizations of sea-surface roughness. In general, each of the five models involves a weighted integral of the wave spectrum $S(k)$ in the wavenumber k space. They are discussed in the following subsections.

2.2.1 RMS model

The RMS model, originally proposed by Anderson and Meneveau [2] for fractal-like (static) land surfaces, uses the r.m.s. value of SGS height fluctuations to model the SGS surface roughness, i.e.

$$\sigma_\eta^\Delta = \left(\widetilde{\eta^2} - \tilde{\eta}^2 \right)^{1/2} . \tag{13}$$

For a continuous spectrum $S(k)$, this becomes

$$\sigma_\eta^\Delta = \left[\int_{\pi/\Delta}^{2\pi/\lambda_c} S(k)\, \mathrm{d}k \right]^{1/2} . \tag{14}$$

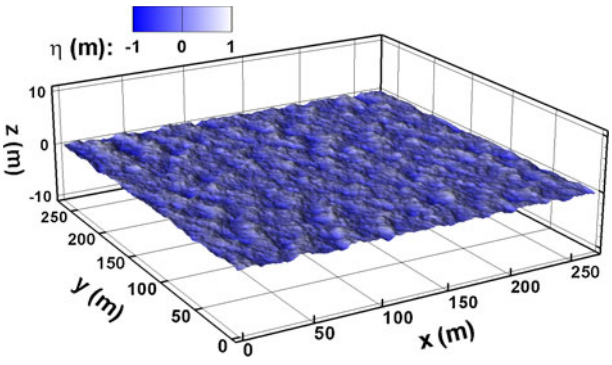

Fig. 1 Three-dimensional sea-surface wavefield for the condition of $U_{10} = 6\,\text{m/s}$ and $F = 50\,\text{km}$. The wavefield is generated based on the JONSWAP spectrum given by Eq. 8. The primary wave propagates along the $+x$-direction

Here, $\lambda_c \simeq 2\,\text{cm}$ is the critical wavelength that separates the gravity and capillary waves [32]. The integral in Eq. 14 is truncated at $k_c = 2\pi/\lambda_c$ since the contribution to the surface stress from the waves shorter than λ_c is negligible [8, 33].

2.2.2 Geometry model

The geometry model parameterizes the SGS surface roughness based on the geometry of the waves. It assumes that for a wave component with wavenumber k, the corresponding roughness is the wave height weighted by a geometry-related function [7]:

$$z_0(k) = \alpha_{w,B} H(k) G(k). \tag{15}$$

Here, $\alpha_{w,B}$ is a coefficient; $H(k)$ is the wave height, which equals to twice of the wave amplitude $a(k)$; and $G(k)$ is the geometric function defined as the ratio of the silhouette area $A_{si}(k)$ to the specific area $A_{sp}(k)$. For a monochromatic wave train, $G(k)$ equals to the wave steepness [7]:

$$G(k) = \frac{H(k)}{\lambda(k)} = \frac{kH(k)}{2\pi}\,. \tag{16}$$

Rewriting Eq. 15 for a continuous wave spectrum $S(k)$ gives the effective amplitude of the SGS waves as

$$\sigma_\eta^\Delta = \int_{\pi/\Delta}^{2\pi/\lambda_c} kS(k)\mathrm{d}k\,. \tag{17}$$

Here, all the scalar prefactors derived from Eq. 15 have been absorbed into the roughness index α_w in Eq. 5 and do not appear in Eq. 17.

2.2.3 Steepness-dependent Charnock model

The steepness-dependent Charnock model is an extension of the original Charnock relation. The Charnock relation [10] states that

$$z_0 = \alpha_{ch} \frac{u_*^2}{g}\,, \tag{18}$$

where the Charnock constant α_{ch} is an empirical coefficient. Previous studies indicate that α_{ch} is dependent on the wave condition instead of being a constant (see e.g. the review by reference [15]). Hsu [21] proposed that the Charnock coefficient α_{ch} in Eq. 18 is dependent on wave steepness. Applying this assumption to the wave component with wavenumber k gives

$$\alpha_{ch} = \alpha_{w,H} \frac{H(k)}{\lambda(k)} = \alpha_{w,H} \frac{kH(k)}{2\pi}\,, \tag{19}$$

where $\alpha_{w,H}$ is a model parameter. Substituting Eq. 19 into Eq. 18 gives

$$z_0 = \alpha_{w,H} kH(k) \frac{u_*^2}{2\pi g}\,. \tag{20}$$

For a wave spectrum $S(k)$, this yields

$$\sigma_\eta^\Delta = \left[2\int_{\pi/\Delta}^{2\pi/\lambda_c} k^2 S(k)\mathrm{d}k\right]^{1/2} \frac{u_*^2}{2\pi g} . \tag{21}$$

It is worth noting that the integrand $k^2 S(k)$ is the slope spectrum of the wavefield.

2.2.4 Wave-kinematics-dependent model

The wave-kinematics-dependent model considers the wave effect on the wind velocity profile in addition to the characteristics of the wave surface geometry. For a wave mode with wavenumber k, Kitaigorodskii and Volkov [29] assumed that the logarithmic wind velocity profile in the frame of reference moving with the wave is

$$U(z) - c(k) = \frac{u_*}{\kappa} \log \frac{z}{\alpha a(k)} . \tag{22}$$

Here, $a(k)$ and $c(k)$ are the amplitude and phase speed of the wave mode k, respectively; and α is a model parameter. Using the dispersion relation for deep water waves, $c(k) = \sqrt{g/k}$, we rewrite Eq. 22 as

$$U(z) = \frac{u_*}{\kappa} \log \frac{z}{\alpha a(k) \exp\left(-\frac{\kappa}{u_*}\sqrt{\frac{g}{k}}\right)} . \tag{23}$$

Therefore,

$$z_0(k) = \alpha a(k) \exp\left[-(\kappa/u_*)\sqrt{g/k}\right] . \tag{24}$$

For a continuous wave spectrum $S(k)$, Eq. 24 suggests [28]

$$\sigma_\eta^\Delta = \left[\int_{\pi/\Delta}^{2\pi/\lambda_c} S(k) \exp\left(-\frac{2\kappa}{u_*}\sqrt{\frac{g}{k}}\right) \mathrm{d}k\right]^{1/2} . \tag{25}$$

2.2.5 Combined-kinematics-steepness model

The combined-kinematic-steepness model combines the concepts of the wave-kinematics-dependent model and the steepness-dependent Charnock model by replacing $H(k)$ in Eq. 20 with the length scale given by Eq. 24 [17]. For a wave spectrum $S(k)$, this gives

$$\sigma_\eta^\Delta = \left[\int_{\pi/\Delta}^{2\pi/\lambda_c} k^2 S(k) \exp\left(-\frac{2\kappa}{u_*}\sqrt{\frac{g}{k}}\right) \mathrm{d}k\right]^{1/2} \frac{u_*^2}{2\pi g} . \tag{26}$$

Based on different aspects of the wind-wave characteristics, the above five candidate models of σ_η^Δ put different weights on the spectral function $S(k)$ in the integration. Figure 2 illustrates the dependence of the integrands on k for each σ_η^Δ model. The following observation can be made:

- The RMS model (Eq. 14) puts uniform weights on all the scales by integrating $S(k)$ directly. It only accounts for the heights of the waves. Note that previous studies on wind–wave interaction show that fast waves exert less drag to wind than slow waves (see the review by Belcher and Hunt [4]). The RMS model is thus expected to be relatively less accurate if the grid resolution is low (i.e. Δ

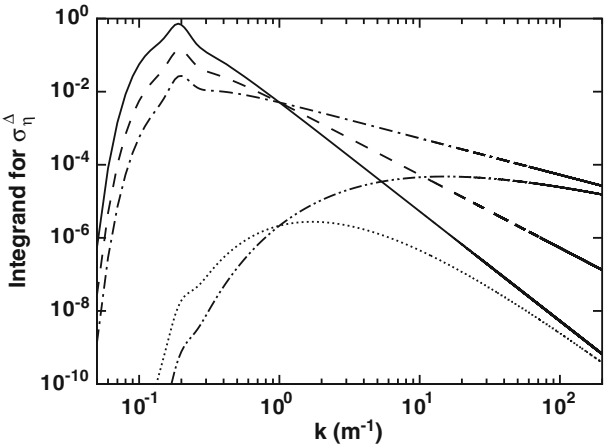

Fig. 2 The integrands in the modeling of σ_η^Δ as functions of k for the condition of $U_{10} = 8\,\mathrm{m/s}$ and $F = 50\,\mathrm{km}$. The values of integrands for various dynamic SGS roughness models are indicated by lines with different patterns: ——, $S(k)$ for RMS model (Eq. 14); – – –, $kS(k)$ for geometry model (Eq. 17); – · –, $k^2S(k)$ for steepness-dependent Charnock model (Eq. 21); · · ·, $S(k)\exp(-2\kappa/u_*\sqrt{g/k})$ for wave-kinematics-dependent model (Eq. 25); and – · · –, $k^2S(k)\exp(-2\kappa/u_*\sqrt{g/k})$ for combined-kinematics-steepness model (Eq. 26). Note that the integrands have different units, i.e.: m^{-3} for $S(k)$ and $S(k)\exp(-2\kappa/u_*\sqrt{g/k})$; m^{-4} for $kS(k)$; and m^{-5} for $k^2S(k)$ and $k^2S(k)\exp(-2\kappa/u_*\sqrt{g/k})$. What are shown in the plot are their dimensional values, and it is thus inappropriate to compare them directly. The purpose of the plot is to show their variation with k with different weights

is large so that the resolved waves propagate fast and behave more differently compared with static roughness elements).

- The geometry model (Eq. 17) also treats the waves as static rough elements. Although the integrand is weighted by k, there is no square-root operator in Eq. 17 as in Eq. 14. As a result, the final value of σ_η^Δ from the geometry model is close to the RMS model because the wind-wave spectrum behaves approximately as $\sim k^{-3}$ (see Eq. 8).
- The steepness-dependent Charnock model (Eq. 26) integrates the slope spectrum $k^2S(k)$, which emphasizes contribution from the short waves (i.e. the high wavenumber part of the wave spectrum) to the SGS sea-surface roughness.
- The wave-kinematics-dependent model (Eq. 25) weights the wave spectrum $S(k)$ by an exponential function $\exp(-2\kappa/u_*\sqrt{g/k})$, which decays rapidly as $k \to 0$. The long waves thus contribute less to the SGS sea-surface roughness than the short waves.
- The weight $k^2\exp(-2\kappa/u_*\sqrt{g/k})$ in the combined-kinematics-steepness model (Eq. 26) simultaneously emphasizes the contribution of the short wave part and reduces the contribution of the long wave part. This combination may appear to be excessive because the integrand is dominated by the short wave part as shown in Fig. 2.

3 Modeling of Wind–Wave Interaction

In this section, we perform a theoretical evaluation of the sea-surface roughness by considering the dynamics of wind–wave interactions. We adopt and extend the

critical-layer theory of Miles [38, 39] to apply it to the case of turbulent wind over JONSWAP wavefield.

3.1 Miles' critical-layer theory

The sea surface is covered by waves that are generated by wind excitation. These waves grow in time and over distance under the wind forcing. An important quantity to describe the wave evolution under wind forcing is the growth rate parameter β, defined as

$$\beta(k) = \frac{1}{\omega(k)e(k)} \frac{\mathrm{d}e(k)}{\mathrm{d}t} \frac{\rho_w}{\rho_a} \left(\frac{c(k)}{u_*} \right)^2 . \tag{27}$$

Here, for the k-th mode, $e(k) = \rho_w g[a(k)]^2/2$ is the wave energy density; ρ_w is the water density; and $\omega(k) = \sqrt{gk}$ is the corresponding angular frequency for deep water waves.

Miles [38] assumed that the wind transfers energy to the wave through the surface form drag associated with the wave-correlated air pressure. By solving the Orr–Sommerfeld equation, Miles [38] obtained the wave growth rate parameter as

$$\beta = -\pi \frac{U_c''}{kU_c'} \frac{\langle w_c^2 \rangle}{u_*^2 \langle \eta^2 \rangle} . \tag{28}$$

Here, the subscript 'c' denotes the value at the critical-layer height $z = z_c$, where the mean wind velocity matches the wave phase velocity, i.e. $U(z_c) = c$; U_c' and U_c'' are respectively the first and second order vertical derivatives of the mean wind velocity at the critical layer; w_c is the vertical velocity at the critical layer; and '$\langle\cdot\rangle$' denotes the horizontal averaging. As shown in Eq. 28, Miles' theory indicates that the wind–wave energy exchange is associated with the mean wind velocity profile at the critical layer, thus is oftentimes referred to as the 'critical-layer theory'. This model has been applied to wave forecasting through the coupling with the third-generation wave prediction model WAM [25].

Miles [39] further improved his original critical-layer theory by including the wave-induced Reynolds stress components. He obtained the wave growth rate parameter for a wave mode k as

$$\begin{aligned} \beta(k) &= \beta_p(k) + \beta_v(k) \\ &= \frac{\pi \zeta_c(k)}{\kappa^2} \log^4\left[\frac{\zeta_1}{\zeta_c(k)} \right] \mathcal{H}[\zeta_1 - \zeta_c(k)] + 2\log\left[\frac{\zeta_1}{\zeta_c(k)} \right] . \end{aligned} \tag{29}$$

Here, $\beta_p(k)$ is the contribution due to wave-induced air pressure variation; $\beta_v(k)$ is the contribution due to the wave-induced Reynolds stress; $\zeta_c(k) = kz_c(k)$ is the dimensionless critical-layer height; $\zeta_1 = e^{-\Gamma}/2 = 0.281$, with Γ being Euler's constant; and

$$\mathcal{H}(z) = \begin{cases} 0, & z < 0, \\ 1, & z \geq 0, \end{cases} \tag{30}$$

is the Heaviside step function.

Note that for different wave modes in a wavefield, the corresponding critical-layer heights are different due to the difference in the phase velocity. Assume the wind turbulence has a logarithmic mean profile

$$U(z) = \frac{u_*}{\kappa} \log\left(\frac{z}{z_0^T}\right) , \tag{31}$$

where z_0^T is the total roughness length of the wave surface. For a wave mode k, matching $U(z_c(k))$ with its wave phase velocity $c(k) = \sqrt{g/k}$ gives the corresponding height of the critical layer as

$$z_c(k) = z_0^T \exp\left(\frac{\kappa}{u_*}\sqrt{\frac{g}{k}}\right) . \tag{32}$$

3.2 Evaluation of sea-surface roughness based on critical-layer theory

We note that the value of the total surface roughness z_0^T in Eq. 32 is unknown beforehand. Meanwhile, it can be related to the total sea-surface stress. For a wavefield with an elevation spectrum $S(k)$, the horizontally averaged total streamwise surface stress acting on the wind is

$$\langle \tau_{13}^T \rangle = -u_*^2 \int_0^{k_c} k^2 \beta(k) S(k)\, \mathrm{d}k - \left[\frac{\kappa\, U(d_2)}{\log\left(\frac{d_2}{z_{0,s}}\right)}\right]^2 . \tag{33}$$

Here, the first term on the right-hand side represents the total form drag due to the waves [25]; the second term represents the viscous shear stress on a smooth surface; and $U(d_2)$ is the mean wind velocity at the height d_2 above the sea surface (i.e. at the first off-surface computational grid point in LES).

On the other hand, $\langle \tau_{13}^T \rangle$ can also be written as

$$\langle \tau_{13}^T \rangle = -\left[\frac{\kappa\, U(d_2)}{\log\left(d_2/z_0^T\right)}\right]^2 . \tag{34}$$

Substituting Eq. 34 into Eq. 33 gives

$$z_0^T = d_2 \exp\left[-\kappa\, U(d_2)\left(u_*^2 \int_0^{k_c} k^2 \beta(k) S(k) \mathrm{d}k + \frac{\left[\kappa\, U(d_2)\right]^2}{\log^2\left(\frac{d_2}{z_{0,s}}\right)}\right)^{-\frac{1}{2}}\right] . \tag{35}$$

Furthermore, for a given wind condition with the value of U_{10} known, the friction velocity u_* and the reference velocity $U(d_2)$ can be obtained by

$$u_* = \frac{\kappa U_{10}}{\log(z/z_0^T)\big|_{z=10}} , \tag{36}$$

$$U(d_2) = \frac{u_*}{\kappa} \log(d_2/z_0^T) . \tag{37}$$

For the theoretical analysis in this study, we choose $d_2 = 0.5$ m, which falls in the range of typical values used in LES of atmospheric boundary layer. Our tests using $d_2 = 0.25$ and 1.0 m show only negligible difference in the results compared with

those obtained using $d_2 = 0.5$ m. Therefore, without losing the generality, we report only the result for $d_2 = 0.5$ m in this paper.

For a given wind and fetch condition (U_{10}, F), an iteration process is required in order to obtain the value of z_0^T for a JONSWAP wavefield with spectrum $S(k)$. The iteration steps are summarized as follows:

(a) Perform an initialization of z_0^T and u_* by solving Eqs. 18 and 36 iteratively, with $\alpha_{ch} = 0.0144$ in Eq. 18 [25].
(b) Calculate the reference velocity $U(d_2)$ using Eq. 37.
(c) Calculate the roughness length $z_{0,s}$ of a smooth surface using Eq. 6.
(d) Calculate the critical-layer height $z_c(k)$ for each wave model using Eq. 32.
(e) Calculate the growth rate parameter $\beta(k)$ for each wave mode using Eq. 29.
(f) Calculate the total sea-surface roughness z_0^T using Eq. 35.
(g) Calculate the friction velocity u_* using Eq. 36.
(h) Repeat steps (b)–(g) until the relative error of z_0^T between the current and the previous iteration steps is small enough. In this study, a threshold of 10^{-8} is used.

In this paper, four different wind conditions are considered, namely $U_{10} = 4$, 6, 8, and 10 m/s. For each wind condition, a range of fetch F is considered, from 0.5 to 500 km. The results obtained by the above approach are shown in Figs. 3 and 4. A variety of experimental results and parameterizations are also plotted for comparison.

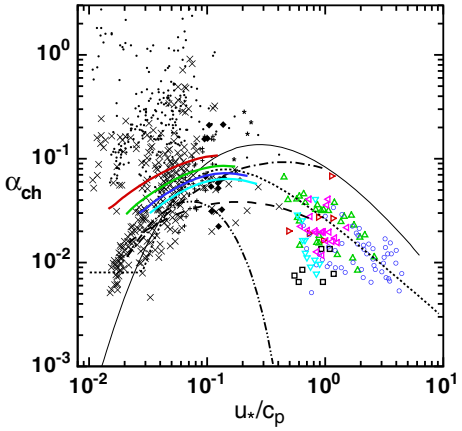

Fig. 3 The Charnock coefficient $\alpha_{ch} = z_0^T g/u_*^2$ as a function of the reversed wave age u_*/c_p. Here, z_0^T is the total surface roughness; u_* is the wind friction velocity; and c_p is the phase speed of the peak wave in the spectrum. Values from field and laboratory measurements are indicated by symbols: ♦, Kawai et al. [27], field; ⋆, Donelan [14], field; +, Merzi and Graf [37], field; •, Toba et al. [50], field, original data; ×, Toba et al. [50], field, revised by Hwang [24]; ▷, Hamada [19], lab; △, Kunishi [30], lab, ○, Kunishi and Imasato [31], lab; ◁, Toba [48, 49], lab; ▽, Hsu et al. [22], lab; and □, Masuda and Kusaba [34], lab. Values based on parameterizations are indicated by lines: −−, Donelan [15]; − · −, Smith et al. [43]; − · ·−, Taylor and Yelland [47]; · · ·, Volkov [52]; and ——, Hwang [23]. Values obtained from Eq. 35 are indicated by solid lines with different colors for various wind speed: *red*, $U_{10} = 4$ m/s; *green*, $U_{10} = 6$ m/s; *blue*, $U_{10} = 8$ m/s; and *cyan*, $U_{10} = 10$ m/s. For each wind speed, the values along the corresponding line are obtained by varying the value of fetch F from 0.5 km to 500 km

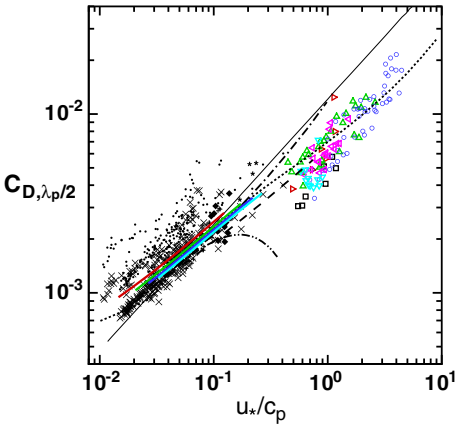

Fig. 4 The drag coefficient as a function of inverse wave age u_*/c_p. Here, $C_{D,\lambda_p/2} = [\kappa/\log(\lambda_p/2/z_0^T)]^2$ is the drag coefficient at the reference height of $z = \lambda_p/2$, with λ_p being the peak wavelength; u_* is the wind friction velocity; and c_p is the phase speed of the peak wave in the spectrum. The meaning of the symbols and lines are the same as in Fig. 3

Figure 3 shows the Charnock coefficient $\alpha_{ch} = z_0^T g/u_*^2$ as a function of $(c_p/u_*)^{-1}$. Here,

$$c_p = \sqrt{g/k_p} \tag{38}$$

is the phase velocity at the spectrum peak. The ratio c_p/u_*, called the wave age [4, 44], indicates to what maturity level the wind-waves have developed. For a fixed wind condition, the wave age c_p/u_* increases as the fetch F increases (cf. Eqs. 10 and 38). As shown in Fig. 3, for each wind condition, the value of α_{ch} obtained from Eq. 35 monotonously increases as u_*/c_p increases up to 10^{-1}, and then slightly decreases as u_*/c_p further increases. As the wind speed increases, the result from Eq. 35 shows a shift of α_{ch} towards larger values. Despite the apparent scattering among the experiment data points, the theoretical prediction from Eq. 35 falls well in the range of experimental data and available, empirical parameterizations.

The effect of sea-surface roughness on the wind turbulence is often quantified using the drag coefficient at a reference height. Figure 4 shows the drag coefficient

$$C_{D,\lambda_p/2} = \left[\frac{\kappa}{\log\left(\frac{\lambda_p/2}{z_0^T}\right)}\right]^2 \tag{39}$$

based on the reference height of $z = \lambda_p/2$, where $\lambda_p = 2\pi/k_p$ is the wavelength at the spectrum peak (see Eq. 10). As shown in Fig. 4, $C_{D,\lambda_p/2}$ increases monotonously as u_*/c_p increases. Unlike z_0^T (cf. Fig. 3), the experimental results of $C_{D,\lambda_p/2}$ display much less scatter when plotted as a function of u_*/c_p. The result from the present analysis based on Eqs. 35 and 39 agrees well with the experimental data and parameterizations.

The analyses and comparisons in this section indicate that the evaluation of sea-surface roughness and drag coefficient based on the latest version of the critical-layer theory [39] provides satisfactory results for a variety of wind speed and fetch conditions. Therefore, we use the results obtained in this section as the benchmark values for the test of dynamic SGS sea-surface roughness models in the next section.

4 Test of Dynamic SGS Sea-Surface Roughness Models

4.1 Mimicking LES data using theoretical prediction

A systematic test is desired to assess the performance of the dynamic SGS sea-surface roughness models. In our previous work, tests have been performed using LES with the dynamic SGS roughness model implemented [2, 3, 57]. Although valuable results were obtained to help evaluating the model performance, these tests had to focus on several representative cases due to the high computational cost required by the LES runs.

In order to cover a wider range of physical parameters, a theoretical test approach is proposed. Instead of being resolved by an LES, the mean GS sea-surface drag $\langle \tau_{13,\Delta}^{GS} \rangle$ in Eq. 1 is modeled using the critical-layer theory discussed in Section 3.1. In that case, the averaged GS and SGS stress on the sea surface can be written as

$$\langle \tau_{13,\Delta}^{GS} \rangle = -u_*^2 \int_0^{\pi/\Delta} k^2 \beta(k) S(k)\, \mathrm{d}k\,, \tag{40}$$

$$\langle \tau_{13,\Delta}^{SGS} \rangle = -\frac{[\kappa\, U(d_2)]^2}{\log^2\left(\frac{d_2}{\sqrt{z_{0,s}^2+(\alpha_w \sigma_\eta^\Delta)^2}}\right)}\,. \tag{41}$$

where the value of $\beta(k)$ is modeled by Eq. 29. The effective SGS wave amplitude σ_η^Δ is modeled by the five candidate models discussed in Section 2.2. The roughness index α_w is obtained by solving the constraint equation

$$\underbrace{-u_*^2 \int_0^{\pi/\Delta} k^2 \beta(k) S(k)\, \mathrm{d}k}_{\langle \tau_{13,\Delta}^{GS} \rangle} \underbrace{-\frac{[\kappa\, U(d_2)]^2}{\log^2\left(\frac{d_2}{\sqrt{z_{0,s}^2+(\alpha_w \sigma_\eta^\Delta)^2}}\right)}}_{\langle \tau_{13,\Delta}^{SGS} \rangle}$$
$$= \underbrace{-u_*^2 \int_0^{\pi/2\Delta} k^2 \beta(k) S(k)\, \mathrm{d}k}_{\langle \tau_{13,2\Delta}^{GS} \rangle} \underbrace{-\frac{[\kappa\, U(d_2)]^2}{\log^2\left(\frac{d_2}{\sqrt{z_{0,s}^2+(\alpha_w \sigma_\eta^{2\Delta})^2}}\right)}}_{\langle \tau_{13,2\Delta}^{SGS} \rangle}\,. \tag{42}$$

We follow Anderson and Meneveau [2] and solve Eq. 42 for α_w using a bisection solution-finding algorithm.

With the value of α_w obtained, the total sea-surface roughness z_0^T can then be calculated by

$$z_0^T = \frac{d_2}{\exp\left[\frac{\kappa\, U(d_2)}{\left(u_*^2 \int_0^{\pi/\Delta} k^2 \beta(k) S(k) \mathrm{d}k + \frac{[\kappa\, U(d_2)]^2}{\log^2\left(\frac{d_2}{\sqrt{z_{0,s}^2+(\alpha_w \sigma_\eta^\Delta)^2}}\right)}\right)^{1/2}}\right]}\,. \tag{43}$$

An iteration procedure similar to the one introduced in Section 3.2 is used here to solve the equations, with the original step (f) being replaced by the above dynamic SGS roughness modeling process (Eqs. 40–43). The five candidate models of σ_η^Δ

introduced in Section 2.2 are tested for the wind and fetch conditions discussed in Section 3.2.

4.2 Test results

Figure 5 shows the GS surface stress $-\langle\tau_{13,\Delta}^{GS}\rangle$ (Eq. 40) as a function of the grid-scale wavenumber k_Δ. As k_Δ increases from zero, the value of $-\langle\tau_{13,\Delta}^{GS}\rangle$ increases gradually and approaches a constant value at very large k_Δ, i.e.

$$\lim_{k_\Delta\to\infty}\left\{-\langle\tau_{13,\Delta}^{GS}\rangle\right\} = u_*^2 - \left[\frac{\kappa\, U(d_2)}{\log(d_2/z_{0,s})}\right]^2 . \tag{44}$$

For all of the cases shown in Fig. 5, the value of $-\langle\tau_{13,\Delta}^{GS}\rangle$ at $k_\Delta = 200\,\mathrm{m}^{-1}$ is already very close to its limit. This confirms that the cut-off wavenumber $k_c = 2\pi/\lambda_c = 314\,\mathrm{m}^{-1}$ for the integrals (e.g. Eqs. 14 and 33) in this study is sufficiently large.

For a fixed fetch F, the value of $-\langle\tau_{13,\Delta}^{GS}\rangle$ increases as the wind speed U_{10} increases, mainly due to the larger wave amplitude under stronger wind (cf. Eq. 9). On the other hand, for a fixed wind condition, the value of $-\langle\tau_{13,\Delta}^{GS}\rangle$ decreases as F increases. This result is consistent with the previous findings that the wave form drag contributes less to the total surface drag as a wavefield evolves to a more matured stage (see e.g. Janssen [26]).

For the test of the dynamic SGS sea-surface roughness models, three different grid-scale filters are considered, namely $k_\Delta = 25$, 50, and $100\,\mathrm{m}^{-1}$, for which the wavenumbers of their corresponding test filters are 12.5, 25, and $50\,\mathrm{m}^{-1}$, respectively. The locations of these filter scales are indicated by the dashed lines in Fig. 5. These filter sizes cover a reasonably wide range of LES grid resolution, which helps to evaluate the resolution effect on the model performance.

The dynamic SGS sea-surface roughness model involves the finding of the roughness index α_w based on Eq. 42. As indicated by Eq. 41, the value of the mean SGS surface stress $\langle\tau_{13,\Delta}^{SGS}\rangle$ (and thus the mean total stress $\langle\tau_{13,\Delta}^{T}\rangle = \langle\tau_{13,\Delta}^{GS}\rangle + \langle\tau_{13,\Delta}^{SGS}\rangle$)

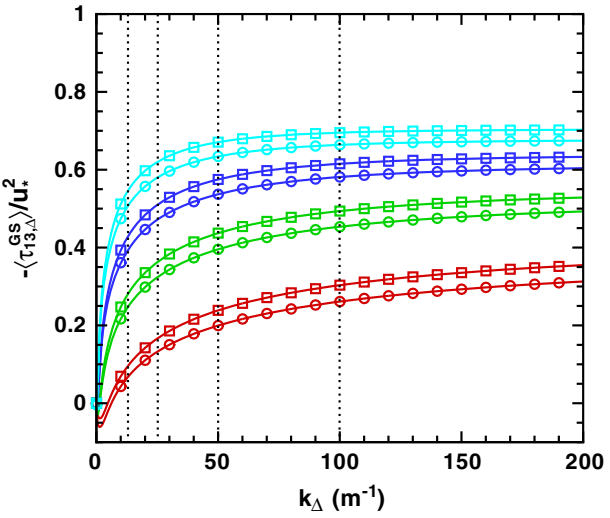

Fig. 5 Surface stress due to GS waves, $-\langle\tau_{13,\Delta}^{GS}\rangle$, as a function of grid-scale wavenumber $k_\Delta = \pi/\Delta$. Here, the value of $-\langle\tau_{13,\Delta}^{GS}\rangle$ is normalized by u_*^2. Various wind speeds are shown and indicated by lines with different colors: *red*, $U_{10} = 4\,\mathrm{m/s}$; *green*, $U_{10} = 6\,\mathrm{m/s}$; *blue*, $U_{10} = 8\,\mathrm{m/s}$; and *cyan*, $U_{10} = 10\,\mathrm{m/s}$. For each wind speed, two fetches are shown and indicated by different symbols: □, $F = 50\,\mathrm{km}$; and ○, $F = 100\,\mathrm{km}$. The locations of $k_\Delta = 12.5$, 25, 50, and $100\,\mathrm{m}^{-1}$ are indicated by dashed lines

depends on α_w. As shown in Fig. 6, $\langle \tau^T_{13,\Delta} \rangle > \langle \tau^T_{13,2\Delta} \rangle$ when $\alpha_w = 0$ because $\langle \tau^{GS}_{13,\Delta} \rangle > \langle \tau^{GS}_{13,2\Delta} \rangle$ (see Fig. 5). When α_w increases, the value of $\langle \tau^T_{13,\Delta} \rangle$ increases at a rate slower than that of $\langle \tau^T_{13,2\Delta} \rangle$ because $\sigma^{\Delta}_{\eta} < \sigma^{2\Delta}_{\eta}$. The point where $\langle \tau^T_{13,\Delta} \rangle = \langle \tau^T_{13,2\Delta} \rangle$ indicates the solution of α_w for Eq. 42.

Figure 6 shows the result obtained from the wave-kinematics-dependent model as an example. For all of the three grid-filter scales considered, the dynamic procedure successfully finds the roughness index α_w that satisfies Eq. 42, indicated by the existence of an intersect between the curves of $\langle \tau^T_{13,\Delta} \rangle(\alpha_w)$ and $\langle \tau^T_{13,2\Delta} \rangle(\alpha_w)$. For each case, the intersect is found at the location where $-\langle \tau^T_{13,\Delta} \rangle(\alpha_w)/u^2_* \approx 1$, indicating that the total surface stress found is indeed the physical value given by the driving force in the wind.

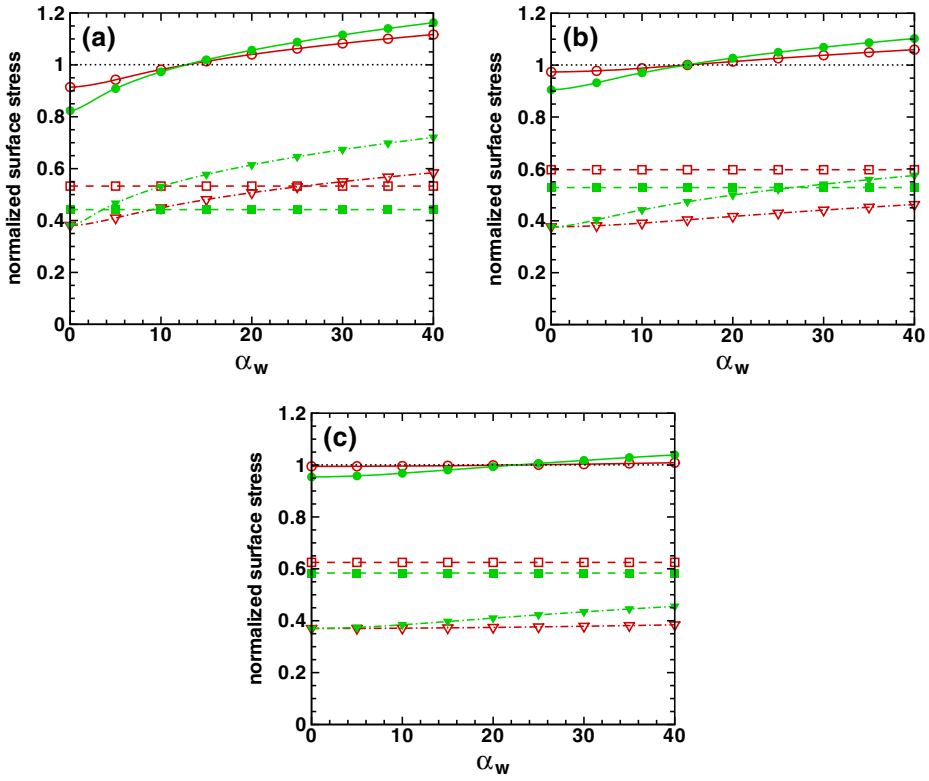

Fig. 6 Total, resolved, and SGS surface stresses as functions of roughness index α_w. The surface stresses are normalized by u^2_*. Results are obtained by the wave-kinematics-dependent model for the condition of $U_{10} = 8$ m/s and $F = 50$ km. Results are shown for both grid-filter scale Δ and test-filter scale 2Δ, with three different values for the grid-filter scale wavenumber $k_\Delta = \pi/\Delta =$: **a** 25 m^{-1}, **b** 50 m^{-1}, and **c** 100 m^{-1}. Values corresponding to grid-filter scale Δ are indicated by *red lines* with open symbols: —○—, total stress $\langle \tau^T_{13,\Delta} \rangle$; – □ –, resolved stress $\langle \tau^{GS}_{13,\Delta} \rangle$; and – · ▽ ·–, SGS stress $\langle \tau^{SGS}_{13,\Delta} \rangle$. Values corresponding to test-filter scale 2Δ are indicated by *green lines* with solid symbols: —●—, total stress $\langle \tau^T_{13,2\Delta} \rangle$; – ■ –, resolved stress $\langle \tau^{GS}_{13,2\Delta} \rangle$; and – · ▼ ·–, SGS stress $\langle \tau^{SGS}_{13,2\Delta} \rangle$

A theoretical value for the SGS surface roughness can be obtained based on the critical-layer theory, similar to the analysis in Section 3.2. Similar to Eq. 33, the SGS surface stress corresponding to filter size Δ can be written as

$$\langle \tau_{13,\Delta}^{SGS} \rangle = -u_*^2 \int_{\pi/\Delta}^{k_c} k^2 \beta(k) S(k)\, \mathrm{d}k - \left[\frac{\kappa\, U(d_2)}{\log\left(\frac{d_2}{z_{0,s}}\right)} \right]^2 , \tag{45}$$

where the value of $\beta(k)$ is given by Eq. 29. Substituting Eq. 45 into Eq. 41 and solving for σ_η^Δ gives

$$\sigma_\eta^\Delta = \frac{d_2}{\sqrt{\exp\left[\frac{2\kappa\, U(d_2)}{\sqrt{u_*^2 \int_{\pi/\Delta}^{k_c} k^2 \beta(k) S(k)\, \mathrm{d}k + \frac{[\kappa\, U(d_2)]^2}{\log^2\left(\frac{d_2}{z_{0,s}}\right)}}} \right]}} . \tag{46}$$

Figure 7 shows the value of σ_η^Δ as a function of grid-filter wavenumber k_Δ. The values obtained from the various models discussed in Section 2.2 are compared with the benchmark value given by Eq. 46. The steepness-dependent Charnock model and the combined-kinematics-steepness model show much smaller decay rates than the benchmark result. Within the range of $k_\Delta \in [10, 100]\,\mathrm{m}^{-1}$ that is relevant to practical LES, the RMS model, the Geometry model, and the wave-kinematics-dependent model show decay rates of σ_η^Δ similar to that of the benchmark result. The correct decay rate of σ_η^Δ with respect to k_Δ, together with a proper value of the roughness index α_w solved by the dynamic procedure, will ensure the success of the model in obtaining a proper SGS sea-surface roughness for use in LES.

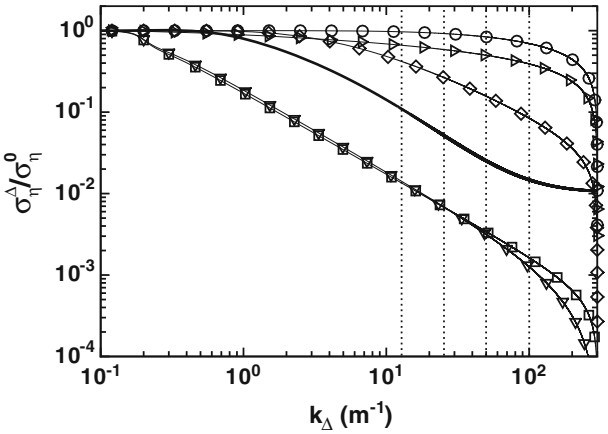

Fig. 7 Effective SGS wave amplitude σ_η^Δ as a function of filter wavenumber k_Δ for the condition of $U_{10} = 8\,\mathrm{m/s}$ and $F = 50\,\mathrm{km}$. Values from various dynamic SGS roughness models are indicated by symbols: □, RMS model; ▽, geometry model; ▷, steepness-dependent Charnock model; ◇, wave-kinematics-dependent model; and ◯, combined-kinematics-steepness model. Based on Miles' critical-layer theory [39], the benchmark value is calculated by Eq. 46. The benchmark is indicated by ——. Normalization is done using the corresponding value of σ_η^0 (the limit of σ_η^Δ as $k_\Delta \to 0$). The locations of $k_\Delta = 12.5$, 25, 50, and $100\,\mathrm{m}^{-1}$ are indicated by *dashed lines*

As pointed above, the overall performance of the dynamic SGS sea-surface roughness model is determined by the combined behavior of both α_w and σ_η^Δ (Eq. 5). Next, we evaluate the performance of the various dynamic SGS roughness models by directly comparing the total roughness length z_0^T, which is shown in Figs. 8 and 9. It is found that, only the combined-kinematics-steepness model fails to converge for $k_\Delta = 25$ and $50\,\mathrm{m}^{-1}$. All of the other dynamic SGS roughness models successfully converge for the range of U_{10}, F, and k_Δ considered in this study.

As shown in Fig. 8, the values of z_0^T obtained from the RMS model and the geometry model are close, with the RMS model agreeing slightly better with the

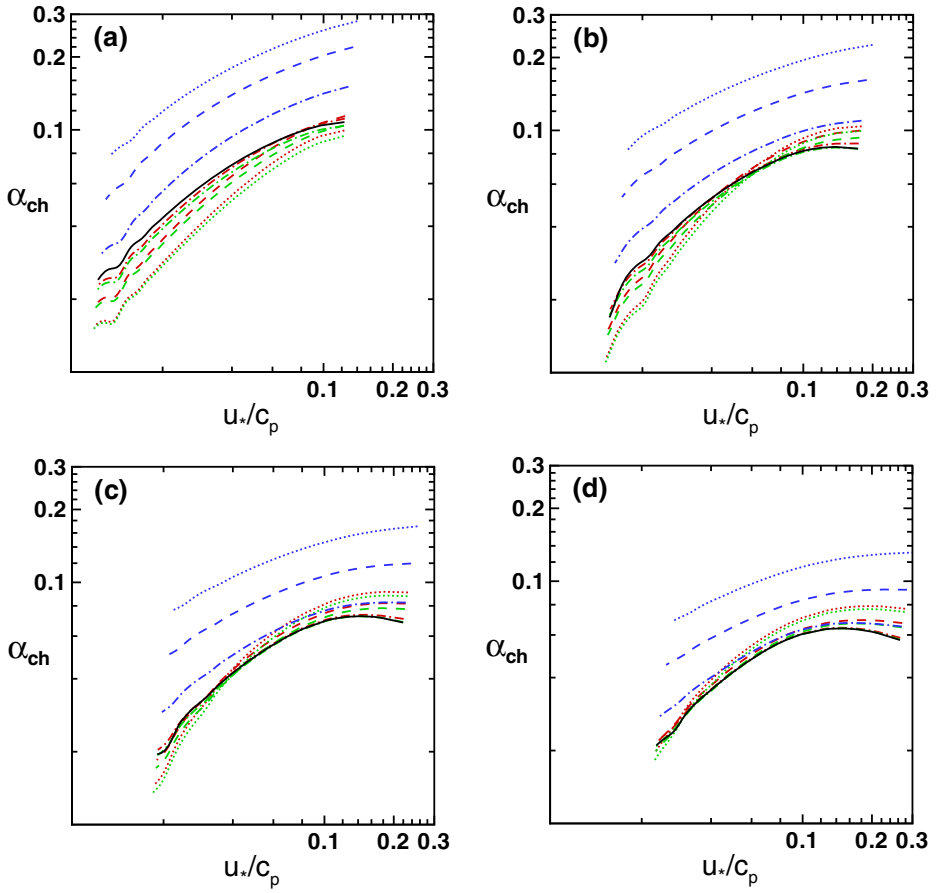

Fig. 8 The Charnock coefficient $\alpha_{ch} = z_0^T g/u_*^2$ as a function of inverse wave age u_*/c_p. Here, z_0^T is the total surface roughness; u_* is the wind friction velocity; and c_p is the phase speed of the peak wave in the spectrum. In the figure, the values in each line are obtained by varying the value of fetch F from 0.5 km to 500 km for a fixed wind speed. Various wind velocities are considered: **a** $U_{10} = 4\,\mathrm{m/s}$; **b** $U_{10} = 6\,\mathrm{m/s}$; **c** $U_{10} = 8\,\mathrm{m/s}$; and **d** $U_{10} = 10\,\mathrm{m/s}$. Values obtained by various dynamic SGS roughness models are indicated by lines with different colors: *red*, RMS model; *green*, geometry model; *blue*, steepness-dependent Charnock model. For each roughness model, values for various grid-filter scale wavenumbers k_Δ are indicated by different line patterns: ——, $k_\Delta = 25\,\mathrm{m}^{-1}$; – – –, $k_\Delta = 50\,\mathrm{m}^{-1}$; and — · —, $k_\Delta = 100\,\mathrm{m}^{-1}$. The benchmark value obtained based on Eq. 35 and Miles' critical-layer theory [39] is indicated by *black solid line*

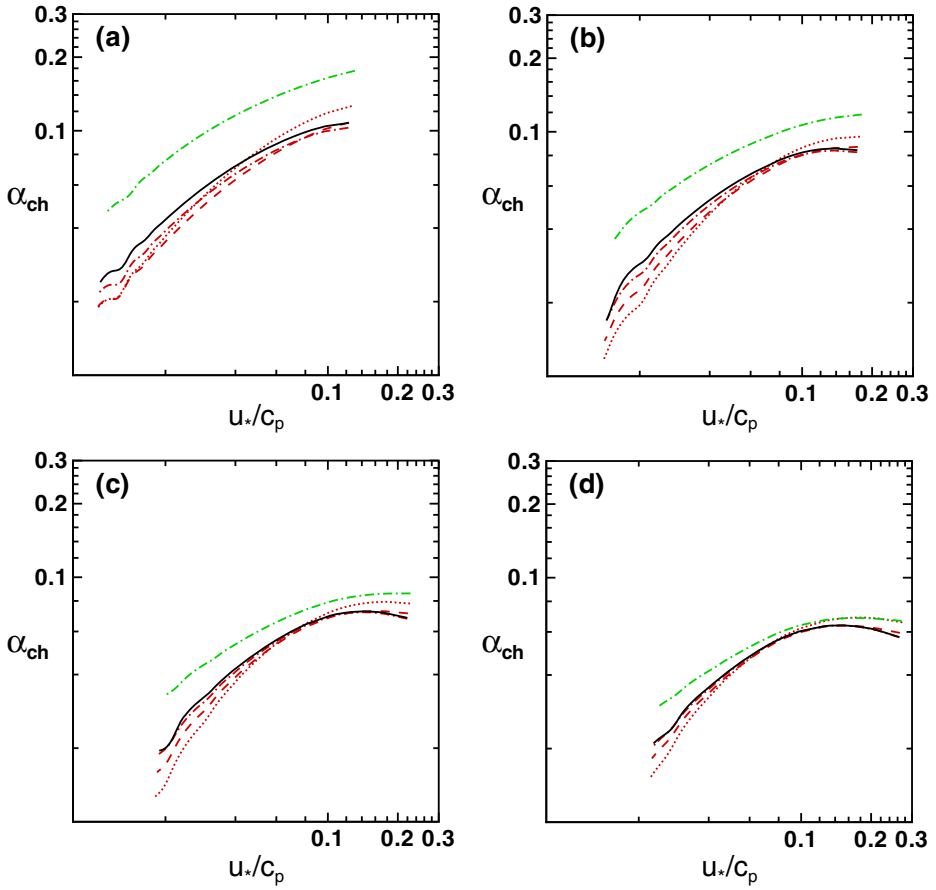

Fig. 9 The same as in Fig. 8 but for the other two dynamic SGS roughness models: *red*, wave-kinematics-dependent model; and *green*, combined-kinematics-steepness model. The benchmark value obtained by Miles' critical-layer theory [39] is indicated by black solid line. The combined-kinematics-steepness model fails to converge for $k_\Delta = 25$ and $50\,\mathrm{m}^{-1}$. Therefore, there are only data from the combined-kinematics-steepness model for $k_\Delta = 100\,\mathrm{m}^{-1}$

benchmark. This is consistent with the result in Fig. 7. For $k_\Delta = 25$ and $50\,\mathrm{m}^{-1}$, the RMS model and the geometry model shows variation in the level of agreement with the benchmark when u_*/c_p changes. In particular, both models underestimate z_0^T for $U_{10} = 4\,\mathrm{m/s}$, but overestimate z_0^T for $U_{10} = 10\,\mathrm{m/s}$. For $U_{10} = 6$ and $8\,\mathrm{m/s}$, both models slightly underestimate z_0^T at small u_*/c_p, but slightly overestimate it at large u_*/c_p. When the grid-filter wavenumber increases to $k_\Delta = 100\,\mathrm{m}^{-1}$, both the RMS model and the geometry model show good agreement with the benchmark. The steepness-dependent Charnock model in general overestimates z_0^T for all of the parameters considered in this study, although acceptable results are obtained for $U_{10} = 8$ and $10\,\mathrm{m/s}$ with $k_\Delta = 100\,\mathrm{m}^{-1}$.

As shown in Fig. 9, the combined-kinematics-steepness model overestimates z_0^T for all the conditions, with fully converged result obtained by the dynamic process only at $k_\Delta = 100\,\mathrm{m}^{-1}$. The wave-kinematics-dependent model achieves the best

overall performance among the five candidate models at all of the four wind speeds. For $k_\Delta = 25\,\mathrm{m}^{-1}$, this model slightly underestimates z_0^T at small u_*/c_p, and slightly overestimates z_0^T at large u_*/c_p. For $k_\Delta = 50\,\mathrm{m}^{-1}$, this model slightly underestimates z_0^T at all u_*/c_p, with better agreement towards large u_*/c_p. The overall performance of the wave-kinematics-dependent model with low k_Δ is better than the RMS model and the geometry model, because of the inclusion of wave kinematics. As k_Δ increases to $100\,\mathrm{m}^{-1}$, the wave-kinematics-dependent model agrees very well with the benchmark.

The results here, together with the discussion and results in earlier sections, consistently indicate that the wave-kinematics-dependent model achieves the best performance among the five candidate models. This conclusion is also consistent with the LES results in reference [57]. Thus the use of the wind-wave kinematics in the modeling of sea-surface roughness associated with the wind-waves appears most desirable.

5 Conclusions and Discussion

In this study, we have discussed the dynamic modeling of the SGS surface roughness in the context of LES of turbulent wind over the ocean wavefield. The modeled SGS roughness has the form $z_{0,\Delta} = \sqrt{z_{0,s}^2 + (\alpha_w \sigma_\eta^\Delta)^2}$, with the dimensionless model coefficient α_w determined by a dynamic approach. The key step of the dynamic model is the enforcement of the constraint that the total sea-surface stress is invariant with respect to the filter scale in the LES. Based on the grid resolution in LES, the sea-surface stress is decomposed into a GS part and an SGS part, with $z_{0,\Delta}$ being included in the SGS stress through a logarithmic surface-layer model. By considering the surface stress at the grid scale Δ and the test scale 2Δ, we obtain a solvable equation to find α_w.

The performance of the dynamic SGS sea-surface roughness model is found to be affected by the modeling of the effective SGS wave amplitude σ_η^Δ, which is modeled as a weighted integral of the SGS wave spectrum based on the wind-wave characteristics. In this study, five candidate models of σ_η^Δ proposed in reference [57] are discussed, namely the RMS model, the geometry model, the steepness-dependent Charnock model, the wave-kinematics-dependent model, and the combined-kinematics-steepness model. A theoretical approach is used for the model tests. Specifically, the GS surface stress is modeled by the critical-layer theory, which is coupled with the dynamic SGS sea-surface roughness model by an iterative solver. This theoretical approach mimics the LES of turbulent wind over sea-surface wavefield in the averaged sense. Its drawback is that it is not directly based on accurate simulations and instead is based on a particular model of the relevant dynamics. But its significant advantage which we exploit here is that its computational cost is significantly lower than directly performing LES, allowing us to test the model performance economically over a much broader range of physical parameters.

The test results indicate that the RMS model and the geometry model obtain satisfactory result, but with the performance at low grid resolution not as good as at high resolution, especially under low wind condition. The steepness-dependent Charnock model as well as its variant, the combined-kinematics-steepness model, show less

satisfactory performance, with the sea-surface roughness apparently overestimated. The wave-kinematics-dependent model achieves the best overall performance among the five candidate models. The agreement with the benchmark is very good. Finally, we remark that these dynamic SGS roughness models are modified from their original forms to fit into the current LES framework for the dynamic modeling of SGS sea-surface roughness.

The present test results apply to the case of the sea-surface roughness models as implemented in LES as SGS models. We recall that they were previously developed for applications other than LES (see Toba et al. [51] for a review), as stand-alone models. We caution that present conclusions about the models' performance do not necessarily translate to their performance as stand-alone models. However, the current theoretical assessment, together with the direct tests using LES [57], provide useful information needed for LES of marine atmospheric boundary layer flows.

Acknowledgements DY and LS acknowledge the support of the Office of Naval Research (grant N00014-09-1-0395). CM acknowledges the support of the National Science Foundation (grant AGS-1045189). Conversations with Dr. William Anderson (now at Baylor University) are also gratefully acknowledged.

References

1. Albertson, J.D., Parlange, M.B.: Surface length-scales and shear stress: implications for land-atmosphere interaction over complex terrain. Water Resour. Res. **35**, 2121–2132 (1999)
2. Anderson, W., Meneveau, C.: Dynamic roughness model for large-eddy simulation of turbulent flow over multiscales, fractal-like rough surfaces. J. Fluid Mech. **679**, 288–314 (2011)
3. Anderson, W., Passalacqua, P., Porté-Agel, F., Meneveau, C.: Large-eddy simulation of atmospheric boundary-layer flow over fluvial-like landscapes using a dynamic roughness model. Boundary-Layer Meteorol. **144**, 263–286 (2012)
4. Belcher, S.E., Hunt, J.C.R.: Turbulent flow over hills and waves. Annu. Rev. Fluid Mech. **30**, 507–538 (1998)
5. Bou-Zeid, E., Meneveau, C., Parlange, M.: A scale-dependent Lagrangian dynamic model for large eddy simulation of complex turbulent flows. Phys. Fluids **17**, 025105 (2005)
6. Bou-Zeid, E., Parlange, M.B., Meneveau, C.: On the parameterization of surface roughness at regional scales. J. Atmos. Sci. **64**, 216–227 (2006)
7. Byrne, H.M.: The variation of the drag coefficient in the marine surface layer due to temporal and spatial variations in the wind sea state. PhD thesis, University of Washington (1982)
8. Caudal, G.: Self-consistency between wind stress, wave spectrum, and wind-induced wave growth for fully rough air–sea interface. J. Geophys. Res. **98**, 22743–22752 (1993)
9. Cavaleri, L., Alves, J.-H.G.M., Ardhuin, F., Babanin, A., Banner, M., Belibassakis, K., Benoit, M., Donelan, M., Groeneweg, J., Herbers, T.H.C., Hwang, P., Jassen, P.A.E.M., Jassen, T., Lavrenov, I.V., Magne, R., Monbaliu, J., Onorato, M., Polnikov, V., Resio, D., Rogers, W.E., Sheremet, A., Smith, J.M., Tolman, H.L., van Vledder, G., Wolf, J., Young, I.: Wave modelling—the state of the art. Prog. Oceanogr. **75**, 603–674 (2007)
10. Charnock, H.: Wind stress on a water surface. Q. J. R. Meteorol. Soc. **81**, 639–640 (1955)
11. Chester, S., Meneveau, C.: Renormalized numerical simulation of flow over planar and non-planar fractal trees. Environ. Fluid Mech. **7**, 195–215 (2007)
12. Chester, S., Meneveau, C., Parlange, M.B.: Modeling of turbulent flow over fractal trees with renormalized numerical simulation. J. Comput. Phys. **225**, 427–448 (2007)
13. Dommermuth, D.G., Yue, D.K.P.: A high-order spectral method for the study of nonlinear gravity waves. J. Fluid Mech. **184**, 267–288 (1987)
14. Donelan, M.A.: On the fraction of wind momentum retained by waves. In: Nihoul, J.C.J. (ed.) Marine Forecasting. Elsevier, Amsterdam (1979)
15. Donelan, M.A.: Air–sea interaction. In: LeMehaute, B., Hanes, D.M. (eds.) The Sea, vol. 9, pp. 239–292. Wiley, New York (1990)

16. Donelan, M.A., Babanin, A.V., Young, I.R., Banner, M.L.: Wave-follower field measurements of the wind-input spectral function. Part II. Parameterization of the wind input. J. Phys. Oceanogr. **36**, 1672–1689 (2006)
17. Geernaert, G.L.: Variation of the drag coefficient and its dependence on sea state. PhD thesis, University of Washington (1983)
18. Germano, M., Piomelli, U., Moin, P., Cabot, W.H.: A dynamic subgrid-scale eddy viscosity model. Phys. Fluids **A3**, 1760–1765 (1991)
19. Hamada, T.: An experimental study of development of wind waves. Technical Report 2, Port and Harbor Tech. Res. Inst. pp. 1–41. Kurihama, Japan (1963)
20. Hasselmann, K., Barnett, T.P., Bouws, E., Carlson, H., Cartwright, D.E., Enke, K., Ewing, J.A., Gienapp, H., Hasselmann, D.E., Kruseman, P., Meerburg, A., Müller, P., Olbers, D.J., Richter, K., Sell, W., Walden, H.: Measurements of wind-wave growth and swell decay during the Joint North Sea Wave Project (JONSWAP). Dtsch. Hydrogr. Z. Suppl. **8**(12), 1–95 (1973)
21. Hsu, S.A.: A dynamic roughness equation and its application to wind stress determination at the air–sea interface. J. Phys. Oceanogr. **4**, 116–120 (1974)
22. Hsu, C., Wu, H., Hsu, E., Smith, R.L.: Momentum and energy transfer in wind generated waves. J. Phys. Oceanogr. **12**, 929–951 (1982)
23. Hwang, P.A.: Influence of wavelength on the parameterization of drag coefficient and surface roughness. J. Oceanogr. **60**, 835–841 (2004)
24. Hwang, P.A.: Drag coefficient, dynamic roughness and reference wind speed. J. Oceanogr. **61**, 399–413 (2005)
25. Janssen, P.A.E.M.: Quasi-linear theory of wind-wave generation applied to wave forecasting. J. Phys. Oceanogr. **21**, 1631–1642 (1991)
26. Janssen, P.: The Interaction of Ocean Waves and Wind. Cambridge University Press, Cambridge (2004)
27. Kawai, S., Okada, K., Toba, Y.: Support of the 3/2-power law and the $gu_*\sigma^{-4}$-spectral form for growing wind waves with field observational data. J. Oceanogr. Soc. Japan **33**, 137–150 (1977)
28. Kitaigorodskii, S.A.: On the calculation of the aerodynamic roughness of the sea surface. Izv. Atmos. Ocean. Phys. **4**, 870–878 (1968)
29. Kitaigorodskii, S.A., Volkov, Y.A.: On the roughness parameter of the sea surface and the calculation of momentum flux in the near water layer of the atmosphere. Bull. Acad. Sci. USSR, Atmos. Ocean. Phys. **1**, 973–988 (1965)
30. Kunishi, H.: An experimental study on the generation and growth of wind waves. In: Disaster Prevention Res. Inst., Kyoto University, Bull., vol. 61, pp. 1–41. Kyoto, Japan (1963)
31. Kunishi, H., Imasato, N.: On the growth of wind waves in high-speed wind flume. In: Annuals, Disaster Prevention Res. Inst., Kyoto University, vol. 9, pp. 667–676. Kyoto, Japan (1966)
32. Lamb, H.: Hydrodynamics, 5th edn. Dover, Mineola (1932)
33. Makin, V.K., Kudryavtsev, V.N., Mastenbroek, C.: Drag of the sea surface. Boundary-Layer Meteorol. **73**, 159–182 (1995)
34. Masuda, A., Kusaba, T.: On the local equilibrium of winds and wind-waves in relation to surface drag. J. Oceanogr. Soc. Japan **43**, 28–36 (1987)
35. Mei, C.C., Stiassnie, M., Yue, D.K.P.: Theory and Applications of Ocean Surface Waves. Part 2: Nonlinear Aspects. World Scientific, Singapore (2005)
36. Meneveau, C.: Germano identity-based subgrid-scale modeling: a brief survey of variations on a fertile theme. Phys. Fluids **24**, 121301 (2012)
37. Merzi, N., Graf, W.H.: Evaluation of the drag coefficient considering the effects of mobility of the roughness elements. Ann. Geophys. **3**, 473–478 (1985)
38. Miles, J.W.: On the generation of surface waves by shear flows. J. Fluid Mech. **3**, 185–204 (1957)
39. Miles, J.W.: Surface-wave generation revisited. J. Fluid Mech. **256**, 427–441 (1993)
40. Moeng, H.: A large-eddy simulation for the study of planetary boundary layer turbulence. J. Atmos. Sci. **41**, 2052–2062 (1984)
41. Monin, A.S., Obukhov, A.M.: Basic laws of turbulent mixing in the ground layer of the atmosphere. Tr. Geofiz. Inst., Akad. Nauk SSSR **151**, 163–187 (1954)
42. Rodriguez-Iturbe, I., Marani, M., Rigon, R., Rinaldo, A.: Self-organized river basin landscapes: Fractal and multifractal characteristics. Water Resour. Res. **30**, 3531–3539 (1994)
43. Smith, S.D., Anderson, R.J., Oost, W.A., Kraan, C., Maat, N., DeCosmo, J., Katsaros, K.B., Davidson, K.L., Bumke, K., Hasse, L., Chadwick, H.M.: Sea surface wind stress and drag coefficients: The HEXOS results. Boundary-Layer Meteorol. **60**, 109–142 (1992)
44. Sullivan, P.P., McWilliams, J.C.: Dynamics of winds and currents coupled to surface waves. Ann. Rev. Fluid Mech. **42**, 19–42 (2010)

45. Sullivan, P.P., Edson, J.B., Hristov, T., McWilliams, J.C.: Large-eddy simulations and observations of atmospheric marine boundary layers above nonequilibrium surface waves. J. Atmos. Sci. **65**, 1225–1245 (2008)
46. Sullivan, P.P., McWilliams, J.C., Hristov, T.: A large eddy simulation model of high wind marine boundary layers above a spectrum of resolved moving waves. In: 19th Conference on Boundary Layer and Turbulence, Keystone, CO (2010)
47. Taylor, P.K., Yelland, M.J.: The dependence of sea surface roughness on the height and steepness of the waves. J. Phys. Oceanogr. **31**, 572–590 (2001)
48. Toba, Y.: Drop production by bursting of air bubbles on the sea surface (III). Study by use of a wind flume. In: Mem. Coll. Sci., Univ. of Kyoto, Ser. A, vol. 29, pp. 313–344 (1961)
49. Toba, Y.: Local balance in the air–sea boundary processes. I. On the growth process of wind waves. J. Oceanogr. Soc. Japan **28**, 109–120 (1972)
50. Toba, Y., Iida, N., Kawamura, H., Ebuchi, N., Jones, I.S.F.: Wave dependence of sea-surface wind stress. J. Phys. Oceanogr. **20** 705–721 (1990)
51. Toba, Y., Smith, S.D., Ebuchi, N.: Historical drag expressions. In: Jones, I.S.F., Toba., Y. (eds.) Wind Stress Over the Ocean, pp. 35–53. Cambridge University Press, Cambridge (2001)
52. Volkov, Y.: The dependence on wave age. In: Jones, I.S.F., Toba, Y. (eds.) Wind Stress Over the Ocean, pp. 206–217. Cambridge University Press, Cambridge (2001)
53. Yang, D., Shen, L.: Characteristics of coherent vortical structures in turbulent flows over progressive surface waves. Phys. Fluids **21**, 125106 (2009)
54. Yang, D., Shen, L.: Direct-simulation-based study of turbulent flow over various waving boundaries. J. Fluid Mech. **650**, 131–180 (2010)
55. Yang, D., Shen, L.: Simulation of viscous flows with undulatory boundaries. Part I: basic solver. J. Comput. Phys. **230**, 5488–5509 (2011)
56. Yang, D., Shen, L.: Simulation of viscous flows with undulatory boundaries. Part II: coupling with other solvers for two-fluid computations. J. Comput. Phys. **230**, 5510–5531 (2011)
57. Yang, D., Meneveau, C., Shen, L.: Dynamic modeling of sea-surface roughness for large-eddy simulation of wind over ocean wavefield. J. Fluid Mech. (2013, in press)